JOURNAL OF GEOPHYSICAL RESEARCH, VOL. 99, NO. C7, PAGES 14,291–14,302, JULY 15, 1994

Estimation of the real aperture radar modulation transfer function directly from synthetic aperture radar ocean wave image spectra without a priori knowledge of the ocean wave height spectrum

S. Jacobsen
Institute of Mathematical and Physical Sciences, University of Tromsø, Tromsø, Norway

K. A. Høgda
Norut Information Technology, Tromsø, Norway

Abstract. The phase and amplitude of the real aperture radar (RAR) modulation transfer function (MTF) are, applying both simulated and real synthetic aperture radar (SAR) image spectra, shown to strongly influence the SAR ocean wave imaging of range- (or near-range) traveling wave systems. Conventionally, in situ measurement of the sea state has been used in connection with SAR estimation of the RAR MTF. In most cases, the SAR imaging has been simulated by varying the phase and amplitude of the transfer function until some criterium for best fit between the measured and simulated spectra is met. The main problem with this method is the need for in situ buoy measurements of the underlying ocean wave height spectrum. This paper proposes a new method for estimating the RAR MTF directly from the SAR ocean wave image spectrum. Hence the method differs from previously used methods in that it is independent of in situ measurements of the sea state. The only (weak) restriction is that the observed wave system is range- or near-range traveling. On the basis of three range-going profiles the RAR MTF phase and amplitude are estimated. Investigations using synthetic data reveal that the SAR image spectrum for realistic sea states is colored by the unknown transfer function to such an extent that the underlying wave spectral form is not critical. Experimentally, the phase and amplitude of the RAR modulation are computed using the Norwegian Continental Shelf Experiment 1988 data. It is shown that the phase is most important for the SAR spectral distribution. Typically, the phase is observed to be in the interval from 60° to 110° and the amplitude to be of the order of 10–18. Furthermore, it is shown from simulation studies that marked changes in real SAR image spectra crossing an atmospheric front are recreated when the measured MTF phase and amplitude are used. Eventually, the hydrodynamic modulation is also extracted from the RAR MTF data. Variations of the hydrodynamic MTF phase across the abovementioned front are focused on. The estimates confirm a consistent wind direction induced modulation on each side of the front. No marked trends are observed for the amplitude. The overall conclusion of the study is that the conformity between simulated and measured spectra is improved when measured RAR MTFs are incorporated in SAR imaging simulation procedures.

1. Introduction

Imaging of ocean waves by synthetic aperture radar (SAR) is strongly influenced by the orbital motion of the scatterers. This is due to the fact that the fine azimuth (along-track) resolution of the SAR is obtained by coherent integration of the backscattered signal. Typically, the integration lasts on the order of seconds and contributes both constructively and destructively to the ocean wave imaging. The constructive effect, denoted velocity bunching, makes it possible to image azimuth-traveling waves. Random motion and spatial decorrelation of the scatterers during the integration interval, together with the nonlinearities of the velocity bunching, contribute destructively to the imaging. Much of the recent work on SAR has been concentrated on these orbital motion effects [*Alpers and Brüning*, 1986; *Alpers and Rufenach*, 1979]. Imaging of range- (cross-track) traveling waves, described by the real aperture radar (RAR) modulation transfer function (MTF), is nevertheless also important.

The RAR MTF is usually divided into terms modeling tilt and hydrodynamic modulation. Tilt modulation is a pure geometric effect describing the variations in backscattered energy due to changes in the local incidence angle of the scattering elements (facets) along the surface waves. Hydrodynamic modulation arises from interactions between Bragg scatterers and long ocean waves. This latter effect produces a nonuniform distribution of the Bragg waves on the sea

Paper number 94JC00633.
0148-0227/94/94JC-00633$05.00

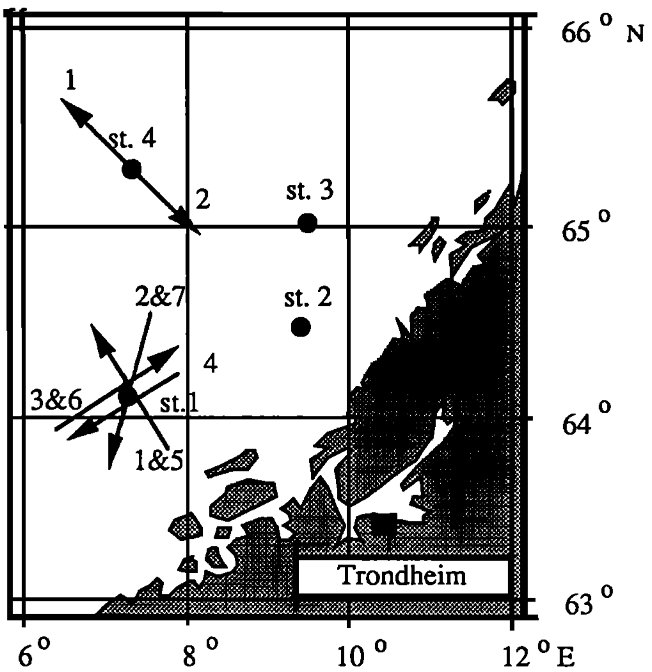

Figure 1. The experiment area of NORCSEX'88 off Norway with buoy locations at stations 1 to 4.

surface. Also contributing, but often neglected, is range-bunching modulation. This modulation arises from the geometric folding of scatterers above or below the mean ocean surface level. Having all these effects in mind, the total RAR MTF is generally assumed to be linearly dependent on the long ocean wave field, although there are extreme cases where this is not a valid assumption [e.g., *Jacobsen and Eltoft*, 1992]. Furthermore, the magnitude and phase of the hydrodynamic MTF are evidently related to air-water interaction mechanisms [*Wright et al.*, 1980; *Plant*, 1986]. Measurements of the hydrodynamic MTF from SAR image spectra will therefore also be a sensitive sensor of air-water interaction processes (see the discussion of atmospheric front in section 5).

Several field campaigns have been conducted to examine the SAR ocean wave imaging process. The Norwegian Continental Shelf Experiment (NORCSEX'88) was carried out in March 1988 at Haltenbanken off mid-Norway (see Figure 1), with participation from Canada, France, Norway, the United States, and Germany. The overall goal of the experiment was to investigate the capability of ERS-1 type of active microwave sensors to measure oceanic features such as near-surface wind, waves, and currents. Several instruments were involved including the Canadian CV-580 X and C band SAR, the Geosat altimeter, and a ship-mounted scatterometer. Only C band (6 GHz) SAR data is processed in this paper. In situ measurements were also collected from wave directional buoys and research vessels.

On March 11, seven SAR flights at two different altitudes were performed. The flights were in a star pattern covering a wave scan buoy. On this day a trimodal wave spectrum with a significant wave height of the order 4–5 m was monitored by the buoy (see Figure 2). On March 20, two of the passes going in opposite flight directions crossed a strong atmospheric front. These data sets give a unique opportunity to study SAR imaging of complex sea states under different imaging geometries and atmospheric conditions.

Using all seven passes from March 11 and the two passes from March 20, SAR image spectra were computed for different incidence angles and ranges. On the basis of these spectra the phase of the RAR MTF, and in most cases the amplitude, were computed with the proposed method. The imaging was then simulated using model and buoy spectra as well as measured and theoretical RAR MTFs as inputs. The results obtained were then compared to corresponding measured SAR image spectra.

It is also of considerable interest to discover the physical mechanisms that influence the modulation of the local radar cross section. It is expected that hydrodynamic interaction theory (section 2.2) is more applicable to decimeter (L band) than centimeter (X and C band) Bragg scatterers. The distribution of the short ripple waves is more affected by the wind than the distribution of longer ones. Wind dependent modulation caused by spatially varying air flow should consequently be expected to occur across an atmospheric front. On the basis of this hypothesis and the assumption that geometrically induced modulation (tilt and range bunching) are modeled correctly (equations (7) and (10)), the hydrodynamic modulation may be extracted from the RAR MTF estimates. Instead of presenting any improved hydrodynamic modulation theory, we apply a simplified model for the hydrodynamic MTF involving a complex amplitude (phase and amplitude) as well as a wavenumber term. This model is thereafter fitted to real SAR data.

In section 2 a short outline of *Hasselmann and Hasselmann*'s [1991] nonlinear integral transform (describing nonlinear SAR imaging) is given, together with some of its implications for imaging in the linear spectral region. In addition, the RAR MTFs conventionally used in the literature are shortly summarized. Section 3 presents the proposed computational procedure for extracting the RAR MTF from SAR image spectra and introduces parameters applied to quantify the procedure performance. Section 4 shortly reviews the NORCSEX'88 experiment including computational procedure, data selection, and supporting in situ

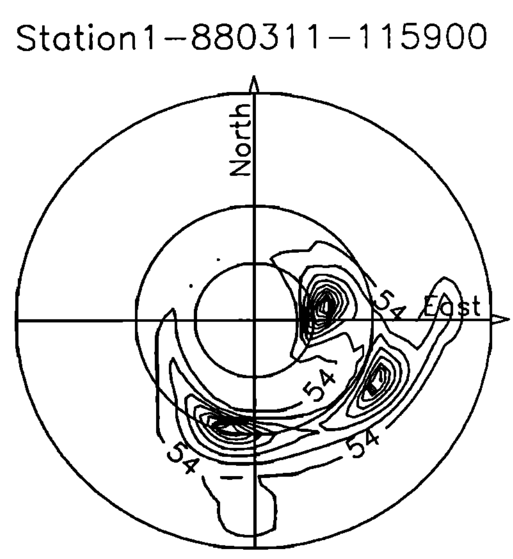

Figure 2. Buoy spectrum from station 1 on March 11 at 1159 UTC.

measurements. Section 5 presents results of obtained RAR MTF estimates for synthetic and real data as well as extraction of the hydrodynamic MTF. Section 6 presents a summary and discussion of the results.

2. SAR Ocean Wave Imaging Model

2.1. The Nonlinear Wave Imaging Transform

Gaussian linear wave theory (GLWT) is assumed to describe the ocean surface properties. Assuming that both tilt and hydrodynamic modulation are linear transformations within GLWT, the SAR image spectrum $S_i(\mathbf{k})$ is given as [*Hasselmann and Hasselmann*, 1991]

$$S_i(\mathbf{k}) = \int_{\mathbf{x}} e^{-i\mathbf{k}\mathbf{x}} G(\mathbf{x}, k_x)\, d\mathbf{x} - I_0^2 \delta(\mathbf{k}) \tag{1}$$

with

$$G(\mathbf{x}, k_x) = I_0^2 e^{-k_x^2[\rho_{\xi\xi}(\mathbf{o}) - \rho_{\xi\xi}(\mathbf{x})]}(1 + \rho_{II}(\mathbf{x}) + ik_x[\rho_{I\xi}(\mathbf{x}) - \rho_{I\xi}(-\mathbf{x})] + k_x^2\{[\rho_{I\xi}(\mathbf{o}) - \rho_{I\xi}(\mathbf{x})][\rho_{I\xi}(\mathbf{o}) - \rho_{I\xi}(-\mathbf{x})]\}) \tag{2}$$

where ρ_{II} is the RAR auto covariance, $\rho_{I\xi}$ is the RAR shift field cross covariance, $\rho_{\xi\xi}$ is the shift field auto covariance, k_x is the azimuth wavenumber, and I_0 is the mean radar cross section.

Equation (2) states that the nonlinear transform contains various combinations of the auto and cross-covariance functions. Numerical implementation of $S_i(\mathbf{k})$ is based on the general form $\rho_{\alpha\beta}(\mathbf{x}) = \mathcal{F}^{-1}(M_\alpha M_\beta^* \Psi(\mathbf{k}))$ of the covariance functions above. Here M refers to a linear transfer function, $\mathcal{F}(\ )$ denotes the Fourier transform, and $\Psi(\mathbf{k})$ is the ocean wavenumber spectrum.

The various terms may be scaled by the nondimensional RAR modulation standard deviation $\mu = [\rho_{II}(\mathbf{o})]^{1/2}$ and the nondimensional azimuth wavenumber $\mathbf{k} = k_x[\rho_{\xi\xi}(\mathbf{o})]^{1/2}$ giving [*Høgda et al.*, 1993]

$$G(\mathbf{x}, k_x) = I_0^2 e^{\mathcal{O}(\kappa^2)}\{1 + \mathcal{O}(\mu^2) + \mathcal{O}(\kappa\mu) + \mathcal{O}[(\kappa\mu)^2]\} \tag{3}$$

Because of the k_x dependence, (1) is not a conventional two-dimensional Fourier transform, and the result turns out to be strongly dependent on the magnitude of κ.

RAR region. When $|\kappa| \ll 1$, $G(\mathbf{x}, \mathbf{k}_x) \approx I_0^2[1 + \rho_{II}(\mathbf{x})]$ yielding a SAR spectrum $S_i(\mathbf{k}) = S_{II}(\mathbf{k})$. Hence the SAR spectrum reduces to the RAR spectrum in this region.

Linear region. For κ up to a size μ we may expand the G function to second order in κ

$$G(\mathbf{x}, k_x) = I_0^2\{1 + \rho_{II}(\mathbf{x}) + ik_x[\rho_{I\xi}(\mathbf{x}) - \rho_{I\xi}(-\mathbf{x})] + k_x^2\rho_{\xi\xi}(x) + \mathcal{O}(\kappa^3)\} \tag{4}$$

After some algebra the linear SAR spectrum is obtained to

$$S_{\text{lin}}(\mathbf{k}) = I_0^2\{|M(\mathbf{k}, \omega)|^2\Psi(\mathbf{k})/2 + |M(\mathbf{k}, -\omega)|^2\Psi(-\mathbf{k})/2\} \tag{5}$$

where M is the combined transfer function $M(k, \omega) = M_I(k, \omega) + ik_x M_\xi(k, \omega)$ and M_I and M_ξ are the RAR and shift transfer functions, respectively.

Nonlinear region. When κ becomes larger than 1, the exponential factor tends to kill all other contributions in G unless $\rho_{\xi\xi}(\mathbf{x})$ is close to $\rho_{\xi\xi}(\mathbf{o})$. For realistic sea states this will occur around $\mathbf{x} = \mathbf{o}$. Thus G might be approximated by

$$G(\mathbf{x}, k_x) = I_0^2[1 + \rho_{II}(\mathbf{0})]e^{-k_x^2[\rho_{\xi\xi}(\mathbf{x}) - \rho_{\xi\xi}(-\mathbf{x})]} \tag{6}$$

that is; no explicit information on RAR effects is contained in (6). Apparently, the RAR MTF will be most important in the RAR and linear region (near range) because the smearing will tend to dominate in the nonlinear region. An estimation procedure for the RAR MTF is consequently best adopted in the linear region since nonlinearities may be neglected within this spectral band.

2.2. RAR Modulation Transfer Function

In this subsection we give a short overview of some of the most common RAR MTF models given in the literature. The tilt and range-bunching modulation given in (7) and (10) are explicitly used in section 5.3 to extract the hydrodynamic modulation from the estimated RAR MTF estimates.

Tilt modulation. Tilt modulation is a geometric effect owing to a locally varying facet tilt over the long ocean waves [*Valenzuela*, 1968]. Assuming Bragg scattering to be dominant, the tilt modulation may be expressed [*Alpers et al.*, 1981]

$$M_{\text{tilt}} = \frac{4 \cot \Theta}{1 \pm \sin^2 \Theta} ik_y \tag{7}$$

where the plus and minus signs denote vertical and horizontal polarization, respectively [*Monaldo and Lyzenga*, 1986].

Hydrodynamic modulation. The Bragg scatter energy will vary over the long ocean wave field because of several factors. Wind tends to modulate the small-scale wave field inhomogeneously over the long wave period. The small-scale wave field will feel a locally varying acceleration of gravity owing to the orbital motion of longer waves. Breaking waves also contribute to the scattering process. All these effects require a complex model and several relations have been proposed to describe the hydrodynamic interactions between the short and long surface waves.

Alpers and Hasselmann [1978] used the action balance equation and modeled the hydrodynamic interaction as

$$M_{\text{hydr}}(\mathbf{k}) = \frac{\omega - i\mu}{\omega^2 + \mu^2} 4.5k\omega \cos^2 \phi \tag{8}$$

where $k \cos \phi = k_y$ and μ is a characteristic relaxation time of the system.

A similar transfer function was obtained by *Keller and Wright* [1975] using the transport equation for the energy spectrum of short water waves. *Feindt* [1985] introduced additional empirical feedback terms $\gamma_r + i\gamma_i$ for modeling wind input in wave tank measurements, leading to the following modification of (8)

$$M_{\text{hydr}}(\mathbf{k}) = \frac{\omega - i\mu}{\omega^2 + \mu^2} 4.5k\omega(\cos^2 \phi + \gamma_r + i\gamma_i) \tag{9}$$

Range bunching. The position determination of a scattering object in range direction is accomplished by the time interval between a pulse and the returned echo. This introduces an object misplacement proportional to the vertical position of the object relative to a reference level, i.e., the mean sea level. The misplacement in range direction, for a facet with height η above the reference height, is given as $\delta r = \tan^{-1} \Theta \eta$. It is readily shown that the range-bunching transfer function may be approximated by [*Gower*, 1983]

$$M_{rb}(\mathbf{k}) = \frac{ik_y}{\tan \Theta} \tag{10}$$

Observe that the range-bunching MTF is in phase with the tilt MTF but contains a smaller amplitude unless Θ is very small.

2.3. Selected RAR MTF Model

Brüning et al. [1988, 1992] and *Monaldo et al.* [1992] used the following simplified model to describe the complete RAR MTF:

$$M_r(\mathbf{k}) = k_y A_r \exp(i\eta_r) \tag{11}$$

where A_r is the amplitude and η_r the phase of the combined tilt and (generally unknown) hydrodynamic modulation. Monte Carlo simulations carried out by *Brüning et al.* [1988, 1992] showed that the location of the spectral peak maxima strongly depends on the phase of the RAR MTF (see also Figure 5). The amplitude of the RAR modulation transfer function was not found to be that critical. However, *Johnsen et al.* [1992] observed in inversion studies that application of a too-low amplitude gave inverted ocean wave spectra with artificial growth of spectral energy along the range axis. Hence the amplitude must at least be roughly estimated to obtain trustworthy results. In this paper it is assumed that the tilt and range-bunching modulation, being purely geometric effects, are reasonably well described. On the basis of the discussion above we adopt the RAR MTF model in (11) and a marginally modified version given by

$$M_r(\mathbf{k}) = \frac{k_y^2}{k} A_r \exp(i\eta_r) \tag{12}$$

3. Measurement Procedure for the RAR MTF

3.1. Previous Approaches

A number of experiments with the goal of measuring the hydrodynamic MTF, have been conducted [e.g., *Feindt et al.*, 1986; *Keller and Plant*, 1990]. Such campaigns have usually been carried out in wind-wave tanks and from towers. Typical problems with these types of experiments are nonrealistic sea conditions in wave tanks and disturbances from towers making downwind measurements impossible. Unfortunately, similar measurements have not yet been carried out at open oceans with wavenumber scales applicable for SAR imaging.

Measurements using SAR have been reported only by a few authors [*Brüning et al.*, 1992, 1993; *Monaldo et al.*, 1992]. These methods have been realized by using some buoy-measured, or wave model obtained, sea surface truth spectra as input for simulation of the SAR imaging process. The RAR MTF is thereafter typically obtained by varying the RAR phase and amplitude A_r and η_r, respectively, until the output spectrum in some way best agrees with the real SAR spectrum. A problem with this method is the dependency of correct information on the sea surface truth. Owing to the strong bandpass structure of the nonlinear SAR imaging transform, small directional mismatches in the input spectrum will give large deviations and misplacement in the energy distribution of the simulated spectrum. The uncertainty of the angular distribution that in fact exists in a buoy spectrum can therefore give large deviations between the true and estimated RAR MTF. In some cases, estimates are impossible, or at least very difficult, to attain.

In this paper we consequently assume that four unknowns have to be dealt with, namely, the phase and amplitude of the RAR MTF and the ocean wave spectrum as well as the azimuth smearing effect. This seems to be a rather difficult problem to handle. However, operating in the quasi-linear region (near range) of the imaging process, several possibilities for estimating the RAR MTF exist, since the parameter then strongly alters the resultant SAR image spectrum.

3.2. Range Profile Method

The proposed method uses three different SAR spectral lines with a constant azimuthal wavenumber value in each line. It is assumed that the imaged ocean wave spectrum is constant (or described by a modeled directional distribution) over the three lines. Using lines on and adjacent to the range axis, it is assumed that the imaging is quasi-linear. These assumptions give rise to several sources of error. Firstly, the ocean wave spectrum is strictly not constant over the profiles. Secondly, outside the range axis the imaging is often nonlinear or at least quasi-linear. However, simulation studies (see section 5.1) using realistic sea states and a priori known RAR MTFs, nevertheless do show that these effects do not influence the estimates significantly. Assume the following linear imaging model (see (5)):

$$S_i = |M_v + M_r|^2 \Psi = [|M_v|^2 + A_r^2 + 2|M_v| A_r \cos(\eta_r - \eta_v)]\Psi \tag{13}$$

where $|M_v|$ and η_v are the velocity-bunching transfer function amplitude and phase, respectively. The velocity-bunching transfer function is well known and takes the form [*Alpers et al.*, 1981]

$$M_v = \frac{R}{V} k_x (gk)^{1/2} \left(i \frac{k_y}{k} \sin \Theta - \cos \Theta \right) \tag{14}$$

where R is the radar-target range and V is the aircraft flight velocity. For range-going waves, that is $k_x = 0$, (13) reduces to $S_i = A_r^2 \Psi$.

Three different lines, $S_{i0} = S_i \delta(k_x)$, $S_{i1} = S_i \delta(k_x + \Delta k)$, and $S_{i2} = S_i \delta(k_x - \Delta k)$ are selected giving the following three equations:

$$S_{i0} = |M_r|^2 \Psi_0 \tag{15}$$

$$S_{i1} = F|M_v + M_r|^2 \Psi_1 \tag{16}$$

$$S_{i2} = F|M_v + M_r|^2 \Psi_2 \tag{17}$$

where F is an exponential function introduced to account for the azimuth smearing effect (see (3)). A useful expression for Fs argument is given by *Høgda et al.* [1993], $k^2 = k_x^2 (R/V)^2 \omega_0^2 (H_s/4)^2 (1 + \cos^2 \theta)$, where H_s is significant waveheight and ω_0 is the ocean spectral peak radian frequency.

Assuming that $\Psi_0 = \Psi_1 = \Psi_2 = \Psi$ (i.e., constant over the range lines but varying with k_y), solving (15) for Ψ and substituting into (16) and (17) give

$$|M_r|^2 S_{i1} - F|M_v + M_r|^2 S_{i0} = 0 \quad (18)$$

$$|M_r|^2 S_{i2} - F|M_v + M_r|^2 S_{i0} = 0 \quad (19)$$

In general, M_r is a function of k, Θ, A_r, and η_r where the latter two parameters are to be estimated. However, F also affects the equation set especially for large R/V ratios. Thus the problem is now reduced to two equations with three unknowns. Depending on the model used for the RAR MTF, this nonlinear set of equations can be difficult or even impossible to solve analytically. Instead of solving the equation set explicitly, an iterative method is introduced. The scheme is based on a stepwise computation of the total linear transfer function for each phase η_r and amplitude A_r of interest. The transfer function is then combined with S_{i0}, S_{i1}, and S_{i2} in (18) and (19). In real data analysis the right-hand side of these latter equations is not zero, but rather a small-value ε. More specifically, the various estimation approaches are as follows:

Case 1. (In this case, $\kappa \approx 0 \Rightarrow F = 1$, which corresponds to a small R/V, H_s, and ω_0.) Step A_r and η_r to extract $\hat{A}_r$ and $\hat{\eta}_r$ by minimizing $(\varepsilon_1 + \varepsilon_2)/2$. The minimum obtainable numerical values on the right hand side of (18) and (19), respectively, are ε_1 and ε_2.

Case 2. (In this case κ is estimated from meteorological wave model data.) Substitute the estimate $\hat{F}$ into (18) and (19) and solve as in case 1.

Case 3. (Unknown κ) Start with $F = 1$ and generate estimates $\hat{A}_r$, $\hat{\eta}_r$ and $[(\varepsilon_1 + \varepsilon_2)/2]_1$. Step F down to a minimum of 0.90 while new estimates are generated in each step. Pick the solution which minimizes $[(\varepsilon_1 + \varepsilon_2)/2]_i$, where i refers to the step number in F_i.

Regardless of which case we are confronting, phase and amplitude values are typically estimated for 10–15 spectral range bins in the most energetic spectral region (to obtain maximum SNR ratio). The final RAR MTF estimate is generated by averaging over the range bins.

3.3. Performance Parameters

In order to give a quantitative measure of the improved imaging performance that is clearly observed visually by introducing measured RAR MTF, two different parameters are applied. The first one is the conventional correlation coefficient K, which is established by correlating the estimated SAR spectrum based on real data and the simulated SAR spectrum. With values between -1 and $+1$ the correlation coefficient is readily interpreted.

Moreover, we also adopt a parameter based on normalized spectra. Analytically, this parameter may be expressed

$$\Gamma = \int_{\mathbf{k}} |S_S^n(\mathbf{k}) - S_M^n(\mathbf{k})| \, d\mathbf{k} \quad (20)$$

where the superscript n reflects that the total power of both simulated S_S and measured S_M SAR spectra is normalized to one. A perfect fit corresponds to $\Gamma = 0$. Cases of no overlap, corresponding to no similarities in power spectral distribution, is reflected by values of Γ close to 2.

4. Measurements Based on NORCSEX'88 Data

For testing the algorithm on real SAR data the two data sets from March 11 and March 20 of the NORCSEX'88 experiment were used. To start with, a number of SAR image spectra were computed. In addition, the imaging process was simulated using directional buoy or wave model spectra and conventional literature RAR MTFs as input. Conventional (or standard) RAR MTFs here refer to (7), (8) (with relaxation time $\mu = 0$), and (10). Furthermore, the conformity to real image spectra was then quantified. RAR MTFs estimated from real SAR image spectra were thereafter run through the same procedure. Eventually, improved performance in the SAR imaging was established.

Table 1. In Situ Measured Air and Sea Conditions

Parameter	March 11	March 20	
$H_{1/3}$, m	4.25	5	
Peak wavelength, m	127	240	
Peak propagation direction, deg[a]	119	230	
Sea temperature, [°C]	6.7	5.7	
Air temperature, [°C]	−0.2	3.7	
Wind direction, deg[a]	352	227[b]	345[c]
Wind speed, m/s	7.5	12.5[b]	5.5[c]

[a]Measured clockwise from north.
[b]High-(up) wind side.
[c]Low-(down) wind side.

4.1. In situ Parameters

The in situ wave and meteorological conditions were measured from four metocean buoys. The geographical site of the experiment is shown in Figure 1. The time of the SAR flights was from approximately 1100 to 1400 on March 11 and from 0730 to 0900 on March 20.

The metocean buoys were deployed to measure both heave and directional ocean wave spectra, in addition to a set of meteorological parameters: wind speed and direction, air and sea temperatures, and air pressure. Details relevant for the analysis are given in Table 1. The buoy measurements were made with a 3-hour period referenced to synoptic hours (0000, 0300, 0600, 0900 UT, etc.). Figure 2 shows the buoy wave spectrum during the March 11 SAR overflights, indicating a rather complex sea state composed of a trimodal swell and wind-wave system. The propagation directions and peak wavelengths for the three modes are 76°, 240 m; 119°, 127 m; and 194°, 156 m, whereas the relative peak power ratios are 0.44, 1.0, and 0.68.

The spectrum was processed using a maximum entropy estimate for the directional distribution [*Lygre and Krogstad*, 1986]. *Rufenach et al.* [1991] estimated the number of degrees of freedom for the buoy spectra to be approximately 32.

Some problems occurred with the buoys during the NORCSEX'88 field investigation period. At station 4 the tape recorder failed, so that only wave parameters computed in real time and no spectra are available. The wind speed quality is also suspect from that station. Especially on March 20, the wind speed was likely overestimated. Data quality was, however, good for stations 1 and 2.

The SAR overflights on March 20 were concentrated over buoy 4 where the spectral data is lacking. Using the SAR image spectra, the directional spectra from buoy 1 and 2, and the available Argos data from buoy 4, it is possible to reconstruct the directional spectra during the SAR over-

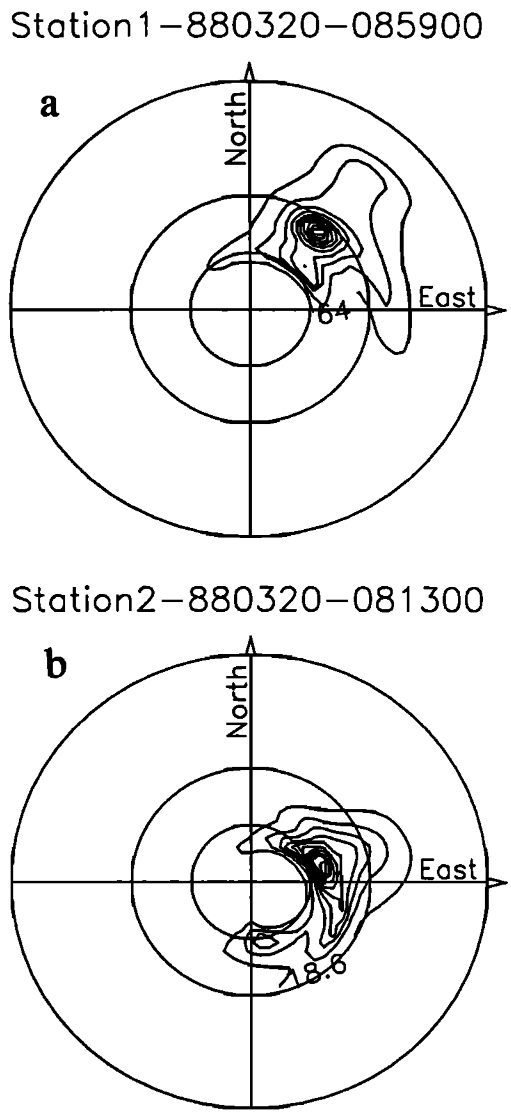

Figure 3. Buoy spectra on March 20. (a) Station 1, 0859 UTC; (b) station 2, 0813 UTC.

flights. At the time of the SAR recording the situation in the area was dominated by a southwesterly system with peak wavelength around 240 m and a northwesterly system with peak wavelength around 110 m. The significant wave height is approximately 5 m. The two-dimensional buoy spectra from stations 1 and 2 are plotted in Figure 3.

The SAR flights were over an atmospheric front that passed through the area. *Mognard et al.* [1991] estimated the wind vector on the high-wind side of the front to be 12.5 ± 1 m/s from 227 ± 5° (clockwise from north) and on the low-wind side to be 5.5 ± 1 m/s from 345 ± 5°.

4.2. SAR Image Spectra Computational Procedure

Some details regarding the real data SAR spectrum estimation procedure are as follows: The real-time CV-580 SAR images were converted to ground range coordinates giving a resolution of 7.7 m in both ground range and azimuth. For March 20, spectra were computed at each side of the front, and for March 11 the spectra were computed as close to station 1 as possible.

For each subimage a two-dimensional illumination function was computed by fitting a polynomial of third order. All range lines were then divided by this polynomial. The subimage power spectra of the fractional image intensity modulation, $(I - \langle I \rangle)/\langle I \rangle$, were estimated using Bartlett's procedure [*Stearns and Hush*, 1990] with 50% overlap and were subsequently smoothed by a quadratic 3 × 3 rectangular-shaped kernel. A total of 31 subimage spectra were used. The final spectrum consists of 256 × 256 spectral values within bins of width δk = 0.0031875 rad/m. The spectra were then corrected for the stationary SAR system response by fitting the Fourier transform of featureless speckle scenes to fourth-order polynomials in both range and azimuth using standard LMS analysis.

5. Results

5.1. Procedure Performance

The importance of the RAR MTF phase is illustrated in Figure 4, which is generated with the SAR simulator described in more detail by *Høgda et al.* [1993]. A left-looking SAR with R/V = 120 s and Θ = 23° is assumed (ERS-1 values). The RAR MTF amplitude A_r is a priori set to 10, whereas the phase η_r is stepped from 0°–150° with a step length of 50°. In Figure 4 the top left spectrum illustrates the simulation with a RAR MTF phase η_r = 0° and bottom right illustrates the simulation with a phase η_r = 150°. A Joint North Sea Wave Project spectrum with Mitsuyasu directional spread [*Mitsuyasu et al.*, 1975], peak wavelength of 200 m, and significant wave height of 4 m is used as input to the simulator. The wind speed input is selected to be 15 m/s. Figure 5 shows the input wave height spectrum. Figure 4 suggests that phase variations in the RAR MTF are capable of completely altering the spectral distribution in the SAR image spectrum.

For testing the reliability of the method with realistic input parameters (variable wave spectrum, nonlinear imaging effects, noise influence on the SAR input spectrum) a simulation study was performed. A number of SAR image spectra were simulated with known RAR MTFs. The resultant SAR image spectrum was then used as input to the RAR MTF computing algorithm and the estimated phase $\hat{\eta}_r$ and amplitude $\hat{A}_r$ were compared to the true values. Starting with a uniform input spectrum (constant for all spectral bins in both range and azimuth) and following the procedure in case 2, we obtain estimates of $\hat{\eta}_r$ and $\hat{A}_r$ with zero bias and variance. Hence the procedure works perfectly since no interfering effects are involved.

Furthermore, the aforementioned synthetic wave spectrum (see Figure 5) was also used as input. The input phase for the simulations was varied from 30° to 180° with 30° step width and amplitude values from 4 to 18 in steps of 2. The ERS-1 R/V ratio and incidence angle were selected (see Figure 4). In addition, the input spectrum was rotated −15° and 15° offset from the range axis to include cases with less azimuthal wave energy. Figure 6 reveals that $\hat{\eta}_r \approx \eta_r$ when A_r is varied (Figure 6a) but that $\hat{\eta}_r$ becomes more uncertain when η_r approaches 180° and A_r is constant (Figure 6c). Furthermore, $\hat{A}_r$ deviates to some degree from A_r when η_r is varied (Figure 6d), and $\hat{A}_r$ becomes biased when $A_r > 10$ (Figure 6b).

These simulations display some of the effects involved in case 3 (section 3.2) and are further illustrated in Figure 7, which depicts typical error surfaces of the RAR MTF phase and amplitude. Solutions of the problem are given by the minimum point in the error surface. When η_r is in the first

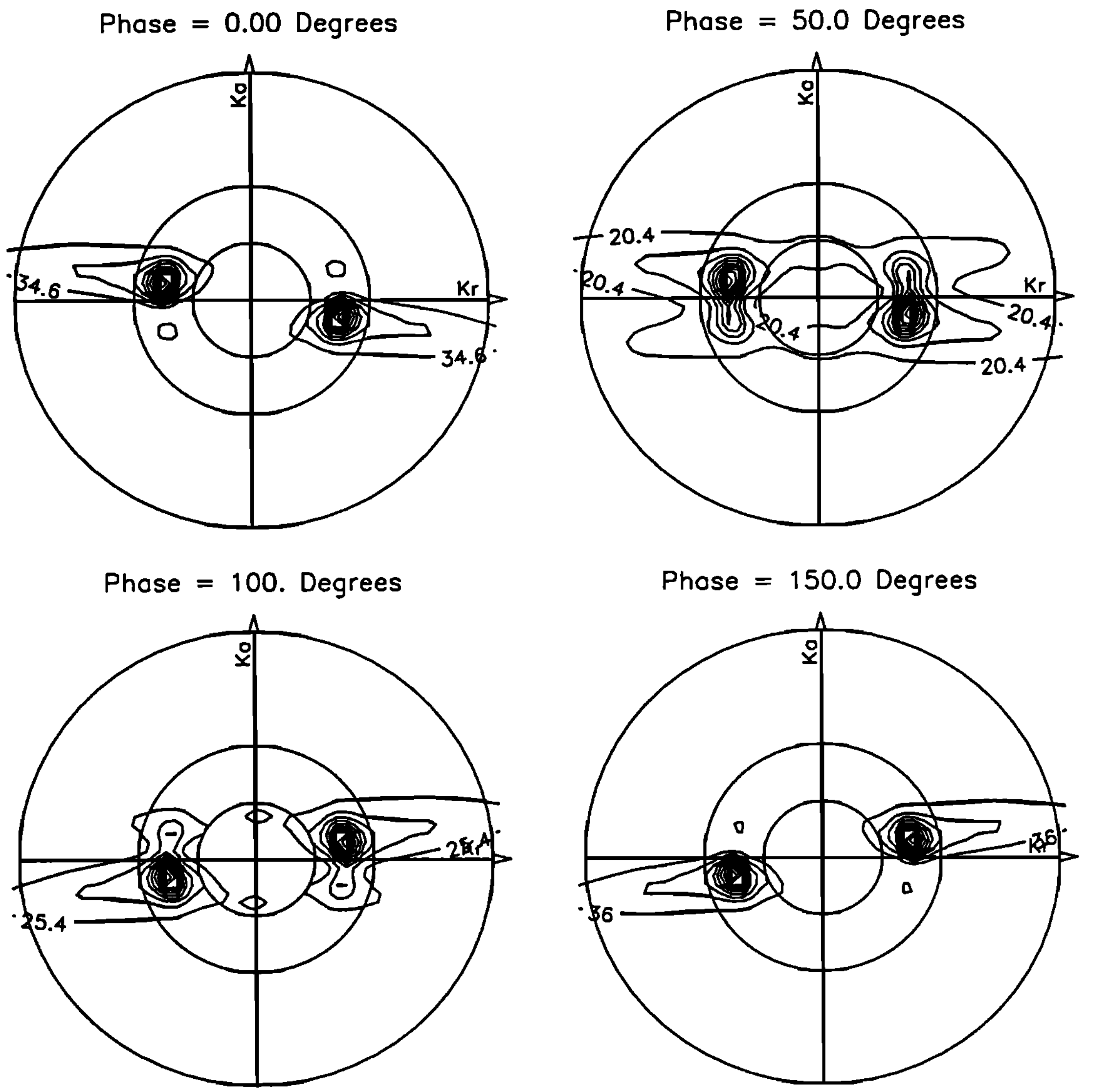

Figure 4. Simulation series of SAR imaging with input spectrum from Figure 5. ERS-1 parameters: R/V = 120 s and Θ = 23°. A_r = 10 and η_r stepped from 0° to 150° with stepwidth 50°.

quadrant the error surface is steep and gives correct results, almost regardless of the amplitude value A_r (see Figure 6a). The gradient in the amplitude direction is smaller giving less performance (see Figures 6b and 6d) for A_r. On the other hand, when η_r is in quadrant 2 (approaching 180°), the error surface contains several local minima. Hence in this case bias effects in both phase and amplitude occur owing to wrong assumptions of a constant Ψ and a linear description.

5.2. RAR MTF Measurements

The next step is to apply the RAR MTF estimator to real data. In scenario 1, we concentrate on data from March 11, which covers a complex trimodal sea state (see Figure 2). Figure 8 shows the complete estimation set of $\hat{\eta}_r$ and $\hat{A}_r$ from this day. The incidence angle and R/V ratio vary from 26° to 76° and 30 s to 177 s, respectively. The data scatter is relatively large, with median values of 13 for the amplitude and 70° for the phase.

In Section 3.3, two performance parameters, namely the correlation coefficient K and an RMS parameter Γ, were introduced. The obtained results in Figure 8 are now evalu ated by these parameters. Figure 9 shows the difference

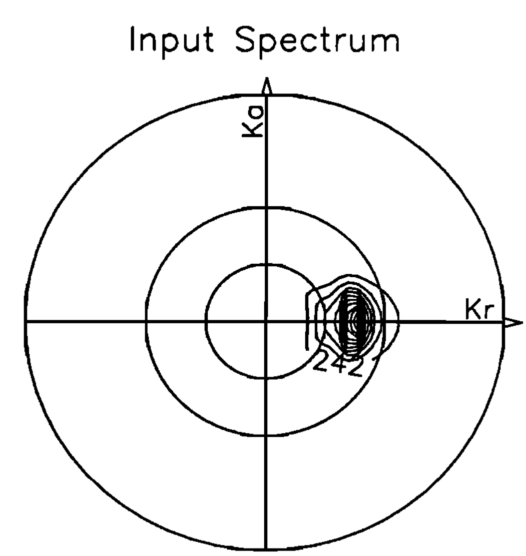

Figure 5. Joint North Sea Wave Project spectrum with *Mitsuyasu et al.*'s [1975] directional spread. Peak wavelength, 200 m; significant waveheight, 4 m; and windspeed, 15 m/s.

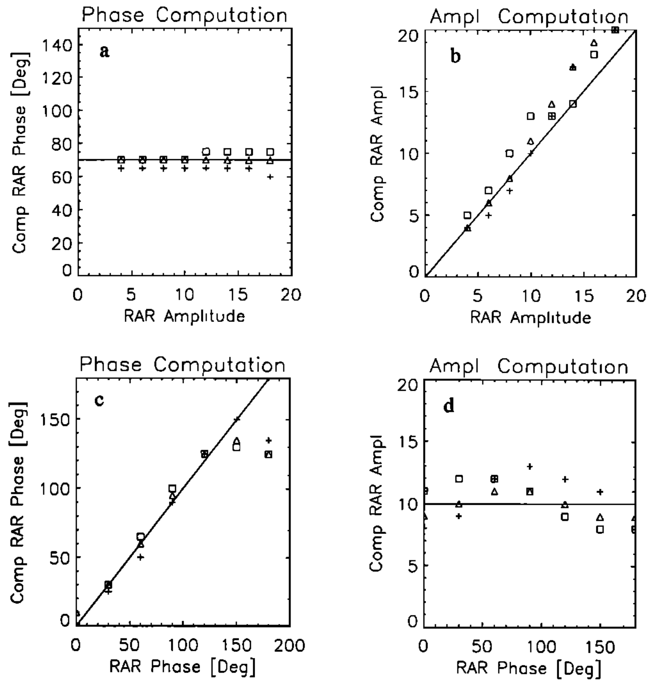

Figure 6. Estimated RAR MTF; (a) $\hat{\eta}_r$ versus A_r with $\eta_r = 70°$; (b) $\hat{A}_r$ versus A_r with $\eta_r = 70°$; (c) $\hat{\eta}_r$ versus η_r with $A_r = 10°$; and (d) $\hat{A}_r$ versus η_r with $A_r = 10$. Triangles represent input spectrum from Figure 4, squares represent +15° clockwise rotation of spectrum, and pluses represent −15° clockwise rotation of spectrum.

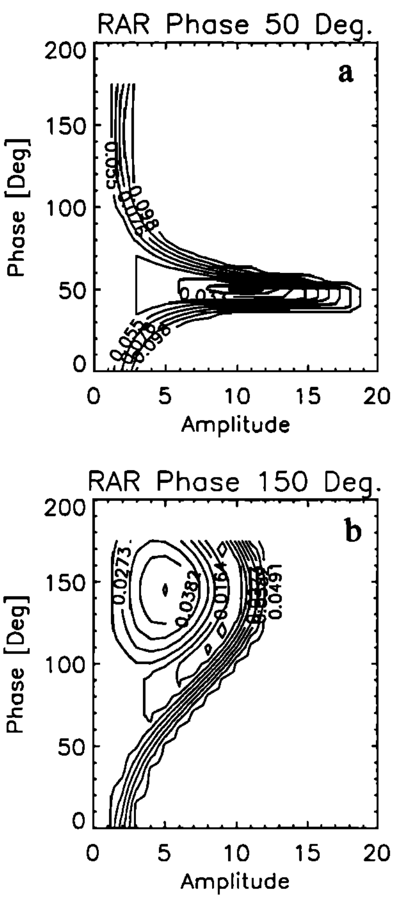

Figure 7. Error surface $((\varepsilon_1 + \varepsilon_2)/2)$ of the RAR MTF estimates. (a) $A_r = 10$ and $\eta_r = 50°$, (b) $A_r = 10$ and $\eta_r = 150°$.

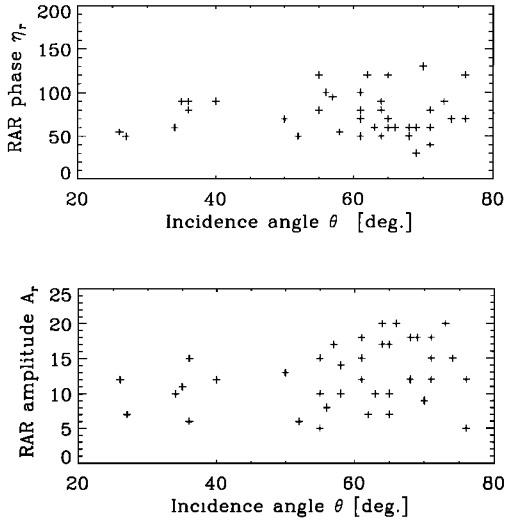

Figure 8. Estimates of RAR MTF phase and amplitude on March 11.

between the performance parameters when standard (subscript s), summarized in section 2.2, and measured (subscript m) RAR MTFs are applied to the simulations. Improved SAR imaging performance is consequently reflected by $\Gamma_m - \Gamma_s < 1$ and $K_m - K_s > 1$. It is evident that better agreement between measured and simulated SAR spectra is obtained by introducing measured MTFs.

No marked trends were observed for the performance parameter with respect to Θ. It therefore makes sense to generate an overall absolute quantification of the results by averaging with respect to the incidence angle. In this manner the following results were obtained: $\langle\Gamma_m\rangle = 0.39$, $\langle\Gamma_s\rangle = 0.64$, $\langle K_m\rangle = 0.75$, and $\langle K_s\rangle = 0.35$, which reflect of the order of 40–55% improved performance.

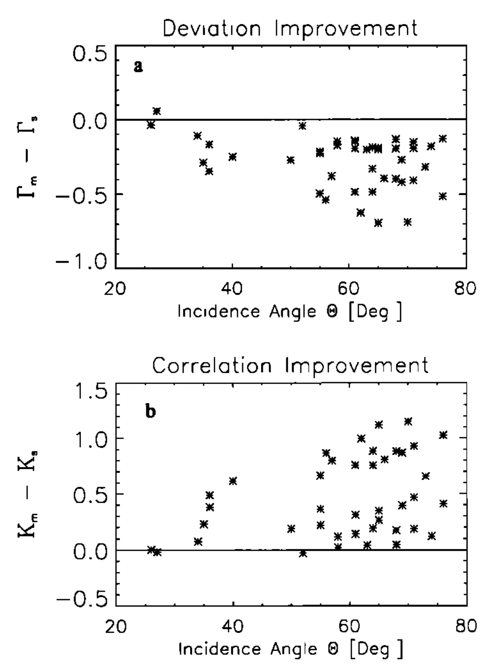

Figure 9. Difference of performance parameters (a) Γ and (b) K on March 11 using standard (s) (equations (7), (8), and (10)) and measured (m) MTFs.

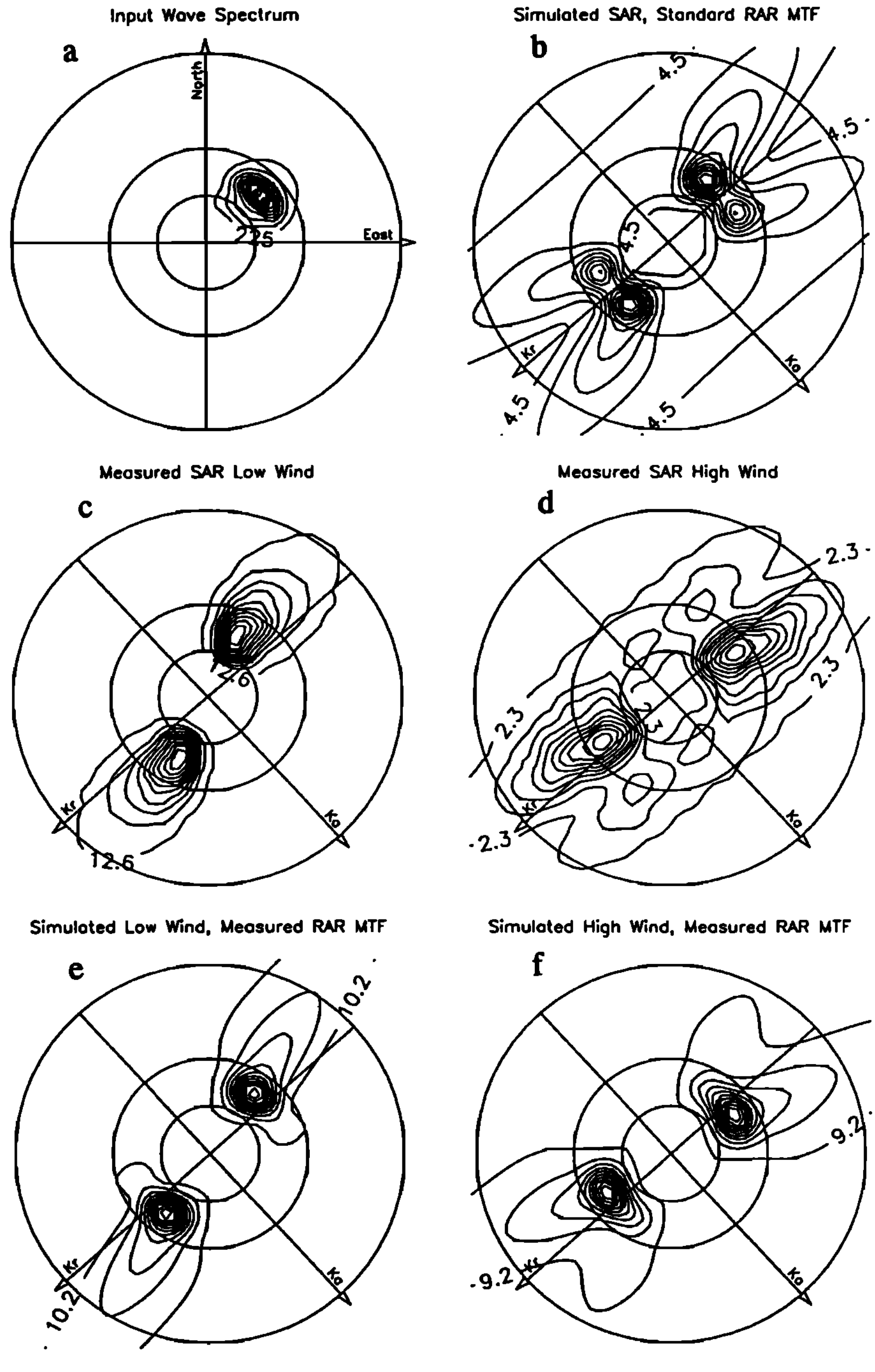

Figure 10. Comparison of simulated and measured SAR spectra (R/V = 60 s and Θ = 30°) on March 20 across atmospheric front. (a) Input ocean wave spectrum. (b) Simulated SAR spectrum using standard literature RAR MTF. Measured SAR spectra on (c) low-wind and (d) high-wind side of front, and simulated SAR spectra (e) low-wind and (f) high-wind side of front with measured RAR MTF.

Scenario 2 contains results from March 20, where the sea state is less complex (see spectra in Figure 3). However, on these overflights the SAR passed an atmospheric front in two opposite lags. The most striking feature with this scenario is the flip of the spectral peak across the range axis when the front is passed (see Figures 10c and 10d). Since the long-wave part of the ocean wave spectrum cannot be rotated over a short propagation distance, this effect is likely to be due to small-scale wind speed dependent modulation. SAR simulation using the standard RAR MTF (see Figure 10b) is not able to reproduce this flipping. However, by generating estimates of $\hat{\eta}_r$ and $\hat{A}_r$, excellent performance is obtained. Visually, this is clear by comparing Figures 10c and 10d with Figures 10e and 10f.

We now generate $\hat{A}_r$ and $\hat{\eta}_r$ for all incidence angles on each side of the front and both lags. Figure 11 depicts the RAR MTF values, and some interesting features appear. Our analysis yields a clustered phase $\hat{\eta}_r$ in the intervals 0° to 40°

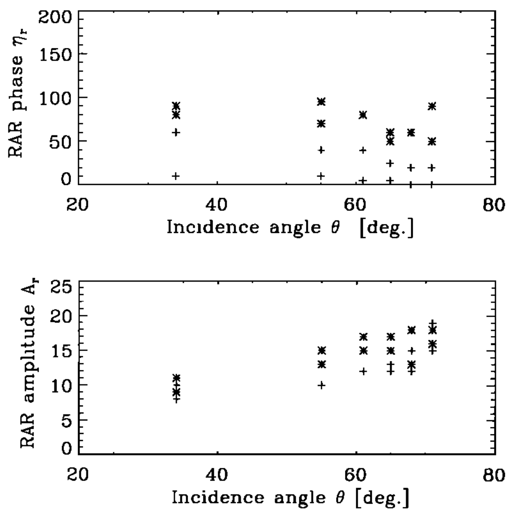

Figure 11. Estimates of RAR MTF phase and amplitude on March 20. Pluses denote downwind and highwind and asterisks denote upwind and lowwind.

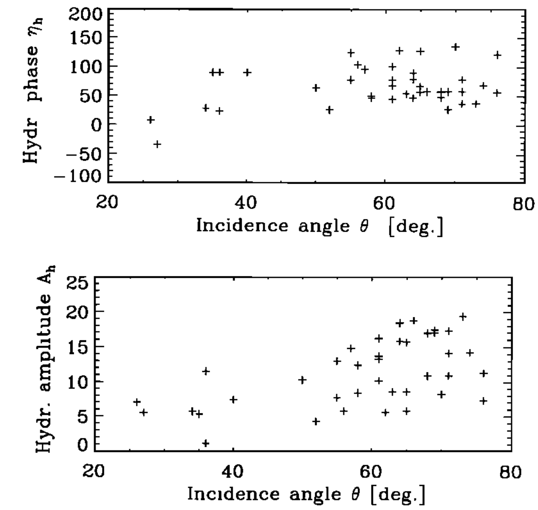

Figure 13. Extracted hydrodynamical MTF phase and amplitude on March 11.

and 50° to 100° in downwind and upwind cases, respectively. The phase also seems to decrease slightly with increasing Θ and R/V. The amplitude A_r is on average smallest on the low-(up) wind side but increases with both Θ and R/V.

As above, it now remains to quantify the imaging performance. Figure 12 is similar to Figure 9 and shows that the SAR simulation is improved for most of the 24 simulations. The estimator uncertainty associated with interfering effects seems to appear as lower performance for large Θ and R/V. Furthermore, the average values of the performance parameters are given by $\langle \Gamma_m \rangle = 0.46$, $\langle \Gamma_s \rangle = 0.67$, $\langle K_m \rangle = 0.76$, and $\langle K_s \rangle = 0.43$, corresponding to an improved performance of 30–45%.

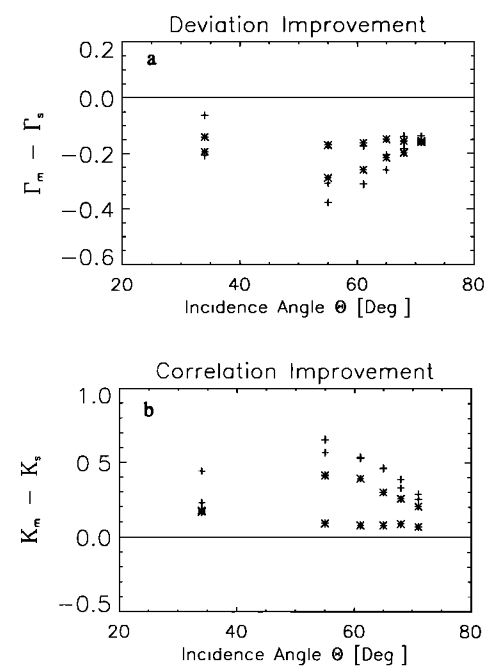

Figure 12. Difference of performance parameters (a) Γ and (b) K on March 20 using standard (s) (equations (7), (8), and (10)) and measured (m) MTFs. Symbols are the same as in Figure 11.

5.3. Extraction of the Hydrodynamic MTF

Assuming that the geometric (tilt and range-bunching) contributions to the RAR MTF are correctly modeled, it is possible to extract the hydrodynamic component from the measurements. This is especially interesting as regards the variations of the hydrodynamic modulation across the front. It is expected that, provided the results are transformed to a given coordinate system at the sea level, the hydrodynamic properties should be relatively constant on each side of the front but variable when passing the front. By putting all the nonspectral information in a complex envelope, the hydrodynamic model in (8) is modified to

$$M_{\mathrm{hydr}}(\mathbf{k}) = A_h \exp(i\eta_h)k_y \tag{21}$$

where A_h is the amplitude and η_h is the phase of the hydrodynamic modulation.

Figure 13 shows the results obtained on March 11. No explicit variations with respect to flight direction or wave propagation direction were observed. Owing to the trimodal sea system on this day, there seems to be no dominant hydrodynamic azimuth modulation angle. However, studying the conditions on March 20, the waves are more directional and the obtained estimates are far more perspicuous. On both the high- and low-wind side, $\hat{A}_h$ is increasing with Θ and R/V. No specific clustering is observed on each side of the front (Figure 14). On the other hand, η_h is clustered according to upwind and downwind modulation. Hence the phase seems to be the governing variable. Relating this feature to simulations (Figure 4) and real SAR spectra (Figure 10), both showing spectral range flipping, this seems to be reasonable.

6. Discussion and Conclusions

A new method for estimating the RAR MTF directly from SAR spectra is introduced. The method is based on using three range lines (on and adjacent to the range axis) that give equations from which the RAR MTF amplitude and phase

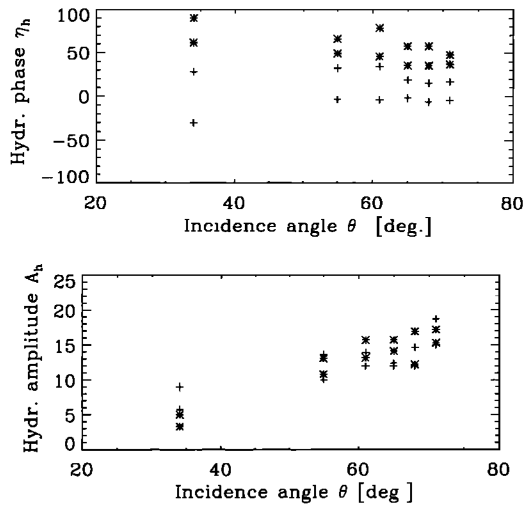

Figure 14. Extracted hydrodynamical MTF phase and amplitude across atmospheric front on March 20. Symbols are the same as in Figure 11.

can be solved. Simulation studies, using a priori known values for the RAR MTF, show that the procedure works well provided compensation for the azimuth-smearing effect is incorporated, although the performance decreases when the phase approaches 180°.

The RAR MTF estimator is also applied on real data taken from the NORCSEX'88 experiment. Two totally different sea states are studied. In scenario 1 a trimodal wave field involving both range and azimuth propagating waves is the basis for the computations. Typical estimates for the RAR MTF amplitude and phase are of the order of 13° and 70°, respectively.

In scenario 2 a flipping of the spectral peak across the range axis (when passing an atmospheric front) is studied. Estimates of the RAR MTF on each side of the front (for two opposite lags) are able to recreate this flipping excellently when applied to SAR simulations. The values obtained for the amplitude A_r lie in the same range as derived from sea-based tower measurements. The phase, however, is different. In cases of parallel wind and wave vectors our analysis yields η_r in the interval of 40° to 100°, whereas tower measurements yield η_r between 20° and 60°. We have no explanations for this discrepancy, which also was observed by *Brüning et al.* [1993]. Furthermore, downwind analysis reveals a clustered phase between 0° and 40°, which is also in accordance with *Brüning et al.* [1993].

In order to quantify the improved performance, which is observed by pure visual inspection when measured RAR MTFs are applied to SAR simulations, two parameters are introduced. One is the conventional correlation coefficient, whereas the other is a RMS type of parameter. Evaluation of all runs in scenarios 1 and 2 shows that the performance is significantly improved (~50%) for both parameters when estimated RAR MTFs are applied.

The variations of the hydrodynamic MTF in these scenarios have also been studied. In scenario 1 the complex trimodal ocean wave spectrum does not seem to generate any dominating hydrodynamic modulation angle, although the wind conditions are steady state. In scenario 2 the unimodal wave spectrum was perturbated by wind-generated modulation on each side of an atmospheric front. The analysis from this day shows a consistent clustering of the hydrodynamic MTF phase. Of main importance here is the relative propagation direction between the wind and the long ocean wave field.

Since the hydrodynamic MTF is an uncontrollable variable it would be tempting to suggest that future SAR systems should be fast, low flying (small R/V), and steep pointing (small Θ) to minimize the azimuth smearing and the hydrodynamic modulation contribution. However, we have observed in our quantitative analysis of SAR imagery the existence of certain specular reflectors appearing as azimuthally oriented streaks. These streaks originate from reflectors with short coherence time (typically 300 ms) dominating within the resolution cell. Since the SAR principle is based on tracking the phase history of the scattering element during the integration time, a short facet lifetime would result in a large Doppler broadening [e.g., *Winebrenner and Hasselmann*, 1988]. This nonlinear effect is not included in *Hasselmann and Hasselmann*'s [1991] transform and will contribute destructively to the modulation and be most important at small incidence angles. Thus there is obviously a tradeoff between minimizing volatile specular reflection and volatile hydrodynamic modulation. An incidence angle of the order of 30°–40° may be a proper choice to prevent dominance from either of these effects. Nevertheless, aiming for an operational SAR inversion system in the future, it seems clear that it is important to establish the RAR MTF, with its coupling to velocity-bunching, in order to correctly model the SAR imaging process.

Acknowledgments. The authors thank the anonymous reviewers for their useful comments. The work was supported in part by the Research Council of Norway, contract SP.27479.

References

Alpers, W., and C. Brüning, On the relative importance of motion-related contributions to the SAR imaging mechanism of ocean surface waves, *IEEE Trans. Geosci. Remote Sens.*, *GE-24*, 873–885, 1986.

Alpers, W., and K. Hasselmann, The two-frequency microwave technique for measuring ocean-wave spectra from an airplane or satellite, *Boundary Layer Meteorol.*, *13*, 215–230, 1978.

Alpers, W., and C. L. Rufenach, The effect of orbital motions on synthetic aperture radar imagery of ocean waves, *IEEE Trans. Antennas. Propag.*, *AP-27*, 685–690, 1979.

Alpers, W., D. B. Ross, and C. L. Rufenach, On the detectability of ocean surface waves by real and synthetic aperture radar, *J. Geophys. Res.*, *86*, 6481–6489, 1981.

Brüning, C., W. Alpers, L. F. Zambresky, and D. G. Tilley, Validation of a synthetic aperture radar ocean wave imaging theory by the Shuttle Imaging Radar-B experiment over the North Sea, *J. Geophys. Res.*, *93*, 15,403–15,425, 1988.

Brüning, C., W. Alpers, R. Schmidt, and K. Richter, The relationship between ocean wave and SAR image spectra studied by Monte-Carlo simulation techniques, in *Proceedings of IGARSS '92*, pp. 1093–1096, IEEE Press, New York, 1992.

Brüning, C., R. Schmidt, and W. Alpers, Ocean wave–radar modulation transfer function inferred from synthetic aperture radar imagery, in *Proceedings of IGARSS '93*, pp. 7–9, IEEE Press, New York, 1993.

Feindt, F., Radar—Rückstreuexperimente Am Wind-Wellen-Kanal Bei Sauberer und Filmdeckter Wasseroberfläche im X Band (9.8 GHz), in *Hamburger Geophysikalische Einzelschriften*, pp. 1–224, G. M. L. Wittenborn, Hamburg, 1985.

Feindt, F., J. Schröter, and W. Alpers, Measurement of the ocean wave–radar modulation transfer function at 35 GHz from a sea-based platform in the North Sea, *J. Geophys. Res.*, *91*, 9701–9708, 1986.

Gower, J. F. R., "Layover" in satellite radar images of ocean waves, *J. Geophys. Res.*, *88*, 7719–7720, 1983.

Hasselmann, K., and S. Hasselmann, On the nonlinear mapping of an ocean wave spectrum into a SAR image spectrum and its inversion, *J. Geophys. Res.*, *96*, 10,713–10,729, 1991.

Høgda, K. A., S. Jacobsen, H. E. Krogstad, and G. Engen, Azimuth smearing in ocean-synthetic aperture radar image spectra: A study of Hasselmann's closed form transformation based on Norwegian Continental Shelf Experiment synthetic aperture radar data, *Radio Sci.*, *28*, 501–512, 1993.

Jacobsen, S., and T. Eltoft, Nonlinear features related to the dual-frequency technique in maritime applications, *Int. J. Remote Sensing.*, *13*(17), 3329–3348, 1992.

Johnsen, H. G., G. Engen, H. E. Krogstad, and S. F. Barstow, Directional wave spectra by inversion of ERS-1 SAR imagery, in Workshop Proceedings of the ERS-1 Geophysical Validation Campaign, 1991, April 27–30, Penhors, Bretagne, France, *Eur. Space Agency Spec. Publ.*, *ESA WPP-36*, 187–192, 1992.

Keller, W. C., and W. J. Plant, Cross section and modulation transfer functions at K_u band measured during the Tower Ocean Wave Radar Dependence experiment, *J. Geophys. Res.*, *95*, 16,277–16,289, 1990.

Keller, W. C., and J. W. Wright, Microwave scattering and straining of wind generated waves, *Radio Sci.*, *10*, 139–147, 1975.

Lygre, A., and H. E. Krogstad, Maximum entropy estimation of the directional distribution in ocean wave spectra, *J. Phys. Oceanogr.*, *16*, 2052–2060, 1986.

Mitsuyasu, H., F. Tasai, T. Suhara, S. Mizuno, M. Ohkusu, T. Honda, and K. Rikiischi, Observation of the directional spectrum of ocean waves using a clover leaf buoy, *J. Phys. Oceanogr.*, *5*, 750–760, 1975.

Mognard, N., J. A. Johannessen, C. E. Livingstone, D. Lyzenga, R. Shuchman, and C. Russel, Simultaneous observations of ocean surface winds and waves by Geosat radar altimeter and airborne synthetic aperture radar during the Norwegian Continental Shelf Experiment, *J. Geophys. Res.*, *96*, 10,467–10,486, 1991.

Monaldo, F. M., and D. R. Lyzenga, On the estimation of wave slope- and height-variance spectra from SAR imagery, *IEEE Trans. Geosci. Remote Sens.*, *GE-24*, 543–551, 1986.

Monaldo, F., T. Gerling, and D. Tilley, A comparison of SIR-B derived wave spectra from hurricane Josephine and wave model predictions, in *Proceedings of IGARSS'92*, pp. 468–470, IEEE Press, New York, 1992.

Plant, W. J., A two-scale model of short wind-generated wave and scatterometry, *J. Geophys. Res.*, *91*, 10,735–10,749, 1986.

Rufenach, C. L., R. B. Olsen, R. A. Shuchman, and C. A. Russel, Comparison of aircraft synthetic aperture radar and buoy spectra during the Norwegian Continental Shelf Experiment of 1988, *J. Geophys. Res.*, *96*, 10,423–10,441, 1991.

Stearns, S. D., and D. R. Hush, Digital Signal Analysis, pp. 380–388, Prentice Hall, Englewood Cliffs, N. J., 1990.

Valenzuela, G. R., Scattering of electromagnetic waves from a tilted rough surface, *Radio Sci.*, *3*, 1057–1066, 1968.

Winebrenner, D. P., and K. Hasselmann, Specular point scattering contribution to the mean synthetic aperture radar image of the ocean surface, *J. Geophys. Res.*, *93*, 9281–9294, 1988.

Wright, J. W., W. J. Plant, W. C. Keller, and W. L. Jones, Ocean wave-radar modulation transfer functions from the West Coast Experiment, *J. Geophys. Res.*, *85*(C9), 4957–4966, 1980.

K. A. Høgda, NORUT Information Technology, Prestvannvegen 98, N-9005 Tromsø, Norway.

S. Jacobsen, Institute of Mathematical and Physical Sciences, University of Tromsø, N-9037 Tromsø, Norway.

(Received September 29, 1993; revised March 7, 1994; accepted March 7, 1994.)